ARTICLE

Cause and Prevention of Moisture-Induced Degradation of Resistance Random Access Memory Nanodevices

Xiang Yang, Byung Joon Choi, Albert B. K. Chen, and I-Wei Chen*

Department of Materials Science and Engineering, University of Pennsylvania, Philadelphia, Pennsylvania 19104-6272, United States

ABSTRACT Dielectric thin films in nanodevices may absorb moisture, leading to physical changes and property/performance degradation, such as altered data storage and readout in resistance random access memory. Here we demonstrate using a nanometallic memory that such degradation proceeds *via* nanoporosity, which facilitates water wetting in otherwise nonwetting dielectrics. Electric degradation only occurs when the device is in the charge-storage state, which provides a nanoscale dielectrophoretic force directing H_2O to internal field centers (sites of trapped charge) to enable bond rupture and charged hydroxyl formation. While these processes are dramatically enhanced by an external DC or AC field and electron-donating electrodes, they can be completely prevented by eliminating nanoporosity, depositing a barrier layer, or using an oxidation-resistant electrode. These findings provide insight for understanding high-performance memory and field-assisted degradation of nanodevices.

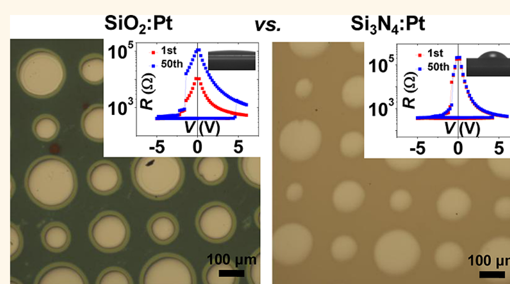

KEYWORDS: nanodevice · nanoporosity · charge transport · dielectric · thin films · dielectrophoresis · functional coatings

Thin films of dielectrics and their hybrids, including ones containing metals, are widely used in electronic and optical nanodevices. Dielectric degradation under ambient conditions has long been recognized as a reliability issue, and it becomes especially important in nanodevices because of nanodimensions. Thin films deposited by physical vapor deposition methods such as sputtering typically are nanoporous with densities lower than theoretical;[1−4] nanoporosity can absorb moisture in the ambient air. This may have a profound influence on the device properties. For example, water with a refractive index $n = 1.3$ can introduce optical mismatch, hence scattering in the film. They can also cause chemical reactions (*e.g.*, forming hydroxides that affect permittivity) or change physical dimensions (*e.g.*, swelling that roughens surfaces).[5] Entrapped moisture can lower the electric resistance of insulating films, even causing electric shorts.[6] It can also create charge-trapping sites, thus affecting device performance.[7,8] Moreover, moisture penetration may extend to the buried layers (*e.g.*, bottom electrodes and substrates), leading to more extended degradation beyond films.

Among dielectric nanodevices of special recent technological interest are ones that exhibit resistive switching properties, thus having the potential of becoming a new class of nonvolatile resistance random access memory (RRAM) materials.[9] Most of these devices switch by forming (soft breakdown) conducting nanofilaments, undergoing redox reactions, or both.[10−16] Naturally, redox reactions are often moisture-sensitive,[17−19] but nanoscale transport may also be environment-sensitive since gas absorption may affect the energetic of ion migration and oxygen activity may affect defect populations that, in turn, affect n/p-type conduction in nanodevices.[20,21] Indeed, for a $Pt/SiO_2/Cu$ RRAM, Tsuruoka *et al.* reported residual water to affect both redox reaction thermodynamics and ion migration kinetics.[18] No such study has been reported for charge-trapping RRAM, however. More broadly speaking, among the very large number of RRAM papers published in recent years, only very few report on this subject.[18,22−26] This is not entirely surprising: many RRAM suffer from large variability in their resistance and switching voltage characteristics,[27−29] which can easily mask the time-dependent effects of environment.

* Address correspondence to iweichen@seas.upenn.edu.

Received for review November 23, 2012 and accepted February 13, 2013.

Published online February 13, 2013
10.1021/nn3054544

© 2013 American Chemical Society

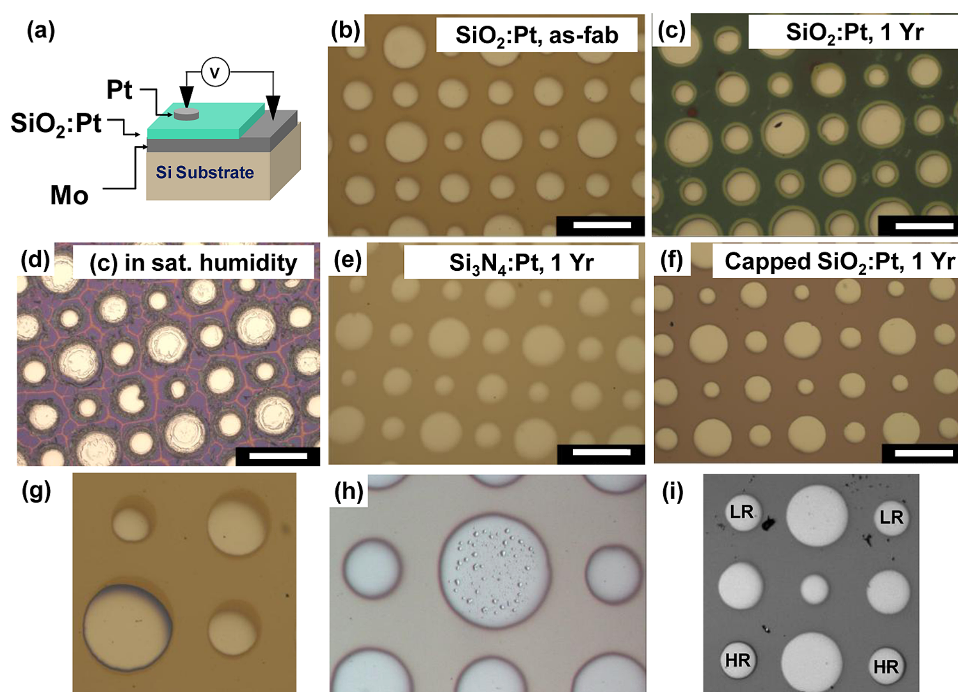

Figure 1. (a) Schematic of nanometallic RRAM device. Active layer (SiO_2:Pt, Si_3N_4:Pt, or Si_3N_4:Cr) sandwiched between top electrode Pt and bottom electrode Mo. Light microscopy image of (b) as-fabricated 80% SiO_2:20% Pt device; (c) device (b) after 1 year in ambient air; (d) device (c) after 3 h in saturated humidity; (e) 95% Si_3N_4:5%Pt device after 1 year in ambient air; (f) Al_2O_3-capped 80% SiO_2:20% Pt device after 1 year in ambient air (scale bar = 250 μm); (g) voltage tested cell (lower left) in 80% SiO_2:20% Pt device showing a dark ring at the cell edge; (h) voltage tested cell (center) in 80% SiO_2:20% Pt device showing bubbles on top electrode; and (i) 80% SiO_2:20% Pt device in different resistance states; dark rings around HRS (lower two, marked) but not LRS (upper two, marked) cells.

In this respect, a recently discovered RRAM based on nanometallic films may provide an excellent platform for studying the moisture effect.[30] These films (5−30 nm thick) are atomic mixtures of random insulators (SiO_2 or Si_3N_4) and metals (Pt, Cr, *etc.*),[30−33] with wave functions of itinerant electrons reaching the full thickness of the films. In the as-fabricated form, these films are conductors. Subsequently, under a voltage trigger, Coulomb barriers arise from trapped charge which blocks the wave functions, so the film switches from the conducting state (the low resistance state, LRS, being the "on state") to a high-resistance (insulating) state (HRS, being the "off state"). This switching process is reversible, and it occurs by an electronic (charge trapping/detrapping) mechanism without forming any filament or Schottky barrier. Our previous work on nanometallic RRAM (made of SiO_2:Pt with a top coat of ∼4 nm Al_2O_3) demonstrated outstanding uniformity of switching characteristics (resistances of HRS and LRS, and on-switching and off-switching voltages).[31−33] In this work, we have systematically investigated the performance of several nanometallic RRAM under various environmental conditions to shed light on the possible degradation mechanisms. In this setting, static and dynamic electric testing is used both to tune degradation kinetics and to probe degradation mechanisms. Solutions to mitigate moisture-induced degradation in these nanodevices have also been demonstrated.

RESULTS AND DISCUSSION

Physical Appearance. In the as-fabricated device (Figure 1a), films of ∼20 nm thick 80% SiO_2:20% Pt film on Mo (bottom electrode)/SiO_2/Si (substrate) had a light tan appearance when photographed under natural light, with the Pt top electrode areas appearing white (Figure 1b). After kept at room ambient conditions for 1 year, the appearance changed to that of Figure 1c, showing dark green films with ring-like features around cells. The evolution of appearance was accelerated by placing the device in a chamber of saturated humidity: the green appearance emerged followed by a violet one after a few hours. This also occurred in films already exposed to air for 1 year: moisture in the chamber of saturated humidity produced the appearance shown in Figure 1d. Such violet color is consistent with the color of MoO_2,[34] which like many other nonstoichiometric MoO_x compounds is a conductor ($x < 3$).[34,35] In contrast, devices made of Si_3N_4:Pt showed no change in appearance when left at room ambient conditions: in Figure 1e is a 1 year old device which looks just like a new one. The SiO_2:Pt device can also become immune to changes if protected by a ∼4 nm Al_2O_3 capping layer, as shown in Figure 1f, after 1 year storage. Likewise, when $SrRuO_3$ was used as the bottom electrode, the SiO_2:Pt device too became immune to change during storage over several years (figure not shown). During electric testing, the (uncapped) SiO_2:Pt device exhibits additional changes

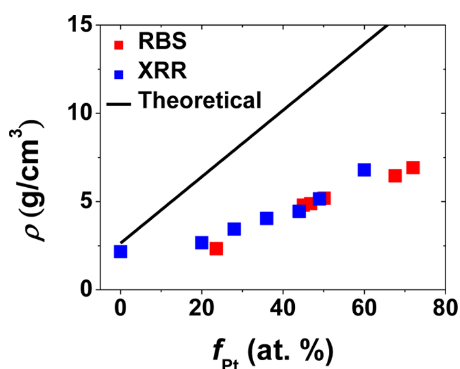

Figure 2. Density of SiO_2:Pt film at various Pt concentration. Data from RBS (red) and XRR (blue). Line: theoretical density $f_{Pt}\rho_{Pt} + (1 - f_{Pt})\rho_{SiO_2}$($\rho_{Pt}$ = 21.46 g/cm^3, ρ_{SiO_2} = 2.64 g/cm^3).

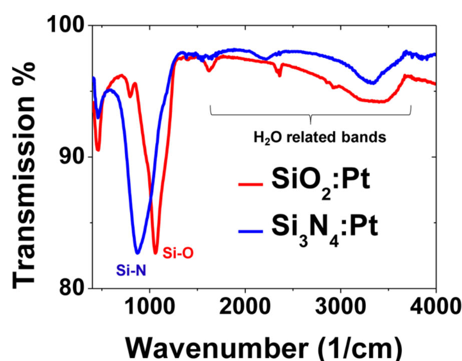

Figure 3. IR spectroscopy of 80% SiO_2:20% Pt and 95% Si_3N_4:5% Pt film from 400 to 4000 cm^{-1}. Strongest Si−N and Si−O stretching bands are labeled. See other band assignments in Table 1.

in appearance. Figure 1g shows the outer edge of a tested cell (lower left) turning dark after one voltage sweep cycle (0 to −5 to 0 to 5 to 0 V); meanwhile, nearby untested cells were unaffected. Such darkening typically occurred during the positive voltage sweep. In addition, these changes sometimes varied from device to device and from cell to cell. For example, some cells experienced "bubble formation" during testing (Figure 1h); these cells could not be switched anymore. If a cell survived the test without change in appearance, during storage, it could still change if left in the HRS, which contains trapped charge. One example is shown in Figure 1i, in which the HRS cells are surrounded by a dark ring and the LRS cells are not. In contrast, SiO_2:Pt films with the same Pt top electrodes but with $SrRuO_3$ bottom electrodes showed no changes during testing (see refs 30 and 31).

Density. According to transmission electron microscopy,[30] all of the films studied here are amorphous, showing no evidence of porosity (low electron density regions). However, density data of SiO_2:Pt films measured by both RBS and X-ray reflectometry, which are consistent with each other as shown in Figure 2, are less than the theoretical ones suggesting nanoporosity. Without incorporating any Pt, sputtered SiO_2 films have a density of ∼2.16 g/cm^3, which is 82% of the theoretical silica density of 2.64 g/cm^3.[3,36] This confirms similar reports of low density for sputtered SiO_2 films.[37] Hybrid SiO_2:Pt films also have a lower density than the theoretical one, taken as

$$\rho_{theoretical} = f_{Pt}\rho_{Pt} + (1 - f_{Pt})\rho_{SiO_2}$$

where f is the atomic fraction of metal, and theoretical densities of pure substances (ρ_{SiO_2} = 2.64 g/cm^3 for silica and ρ_{Pt} = 21.46 g/cm^3 for Pt metal) are used. The relative densities of all of the Pt-containing films in Figure 2 are around 0.5, indicating a highly porous structure, which was also reported for other oxide-metal hybrids.[38] On the other hand, sputtered Si_3N_4 films had a density of 3.48 g/cm^3, close to that of fully dense Si_3N_4 ceramic in the literature.[39] The density of 93% Si_3N_4:7%Cr films, to be used for device study later in this work, had a density of 3.62 g/cm^3, which is only 3% lower than $\rho_{theoretical}$ ($\rho_{Si_3N_4}$ = 3.44 g/cm^3,ρ_{Cr} = 7.19 g/cm^3). This means that Si_3N_4:Cr films are almost free of pores. Other evidence of different nanoporosity in different films came from atomic force microscopy (Figure S1 in the Supporting Information). When area (10 × 5 μm^2) scans of surface topography are compared, SiO_2:Pt film exhibits much larger roughness (1.8 nm rms, consistent with the data in the literature[30]) than Si_3N_4:Cr film (0.29 nm rms).

TABLE 1. IR Absorption Bands of 80% SiO_2:20% Pt

location (cm^{-1})	assignment
463	Si−O−Si rocking
795	Si−O−Si bending
1057	Si−O−Si stretching
1632	bending of free H_2O and/or H_2O H-bonded to silanol
2341	CO_2 vapor
3225	free/H-bonded H_2O
3450	stretching of H_2O bound to silica network
3600	OH stretching of H-bonded silanol groups

IR Spectroscopy. Transmission FTIR spectra of ∼100 nm films deposited on KBr substrates are shown in Figure 3. (These films were left at room ambient conditions for a few days after removal from the sputtering chamber.) The spectra of 80% SiO_2:20% Pt from 400 to 4000 cm^{-1} contain peaks listed in Table 1, in which the three lowest wavenumber ones are Si−O−Si vibration modes while the rest are all environment (H_2O, CO_2) related.[40,41] Similarly, in the 95% Si_3N_4:5% Pt spectra, two characteristic Si−N−Si peaks are identified at lower wavenumbers, while all of the higher wavenumber peaks are probably environment related. (Very similar data were obtained for 93% Si_3N_4:7% Cr, shown in Figure S2, confirming that the peaks are due to Si−N−Si and environmental species and not affected by atomically dispersed metals.) Relative to the strongest characteristic peak (1057 cm^{-1} for Si−O−Si stretching and 870 cm^{-1} for Si−N−Si stretching), most of the environment-related peaks are more prominent in the SiO_2:Pt film, suggesting more H_2O absorption.

Wetting. On sputtered 80% SiO_2:20% Pt nanometallic films (~200 nm, without the top electrode) water wetting is remarkably complete (wetting angle <3°), as shown in Figure 4a: as soon as the water droplet touched the film, it immediately spread out. This is surprising since SiO_2 is not known to be wetting. Indeed, a presumably dense thermal oxide SiO_2 (~200 nm, formed by oxidation of a Si wafer) had a contact angle of ~50° (Figure 4b), which is consistent with the reported data for silica in the literature.[42] Such huge difference in the wetting behavior between sputtered SiO_2:Pt films and dense SiO_2 films is known to occur: a highly porous surface of a hydrophobic substance can become superhydrophilic.[43] Since no visible porosity was found in our films according to microscopy, it must be nanoporosity that causes both lower density and apparent wetting. Similarly, we compared the wetting angles of our sputtered 95% Si_3N_4:5% Pt film (47° in Figure 4c) and a dense hot-pressed SiAlON (in which Al and O partially substitute Si and N in the Si_3N_4 network) ceramic (60° in Figure 4d),[44] observing a similar, though less drastic, increase in wettability in the film, presumably also due to nanoporosity. In contrast, when 80% SiO_2:20% Pt is capped with a Al_2O_3 ALD film (~4 nm), it shows a wetting angle (52°, Figure 4e) close to that of a dense sintered alumina ceramic (50°, Figure 4f), suggesting that the ALD Al_2O_3 film is rather dense. Lastly, 93% Si_3N_4:7% Cr films have the same wetting property (~49° as Si_3N_4:Pt films. These results are summarized in Table 2.

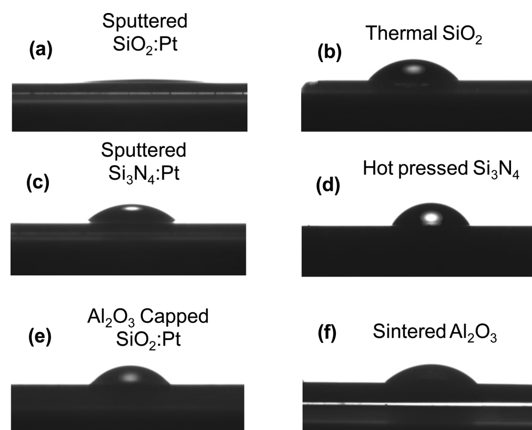

Figure 4. Wetting by static sessile water drop on (a) sputtered 80% SiO_2:20% Pt film; (b) thermally oxidized SiO_2 film; (c) sputtered 95% Si_3N_4:5% Pt film; (d) hot-pressed Si_3N_4 ceramic; (e) ALD Al_2O_3-capped 80% SiO_2:20% Pt film; and (f) sintered Al_2O_3 ceramic. Calculated wetting angles listed in Table 2.

TABLE 2. Wetting Angles of Various Films and Ceramics

sample	setting angle (deg)
sputtered SiO_2:Pt	<3
thermal SiO_2	50
sputtered Si_3N_4:Pt	47
hot-pressed Si_3N_4	60
Al_2O_3-capped SiO_2:Pt	52
sintered Al_2O_3	50

Electric Characterization of 80% SiO_2:20%Pt Films. As-fabricated devices were all in a conducting state with an initial resistance *R* between 10^2 and 10^3 Ω. A typical current−voltage (*I*−*V*) and *R*−*V* cycle are shown in Figure 5a, having the following characteristics. When a forward bias voltage is applied, the current suddenly drops at a certain voltage (~4 V), which transitions the cell to the HRS (the "off" state in RRAM). The cell is "nonvolatile" and "bipolar" in that the HRS is maintained at 0 V and that a reverse bias is required to switch it back to the LRS (the "on" state) through a series of current increases indicating a multistep process. This is in agreement with our previous findings:[30−33] when Pt is used as top electrode and Mo or $SrRuO_3$ as bottom electrode, the switching direction is counterclockwise in the *R*−*V* hysteresis, changing from LRS to HRS at a positive bias and *vice versa* at a negative bias.

Devices made of SiO_2:Pt with Mo bottom electrode and without capping are not stable at the room ambient conditions in the sense that its resistance (especially HRS) changes with time and external voltage. Figure 5b shows the results of a retention test for a device at the HRS (kept at room ambient conditions with a relative humidity 10−15%.) In this experiment, several fresh cells were first switched to the HRS with R_{HRS} ~ 81 kΩ. The resistance of one cell (named cell A) was periodically monitored using a small voltage (0.2 V), while other cells (cells B, C, *etc.*) were used as surrogates for evaluating switchability. (We assume cell A and its surrogates behave similarly as long as they are not disturbed by a voltage sweep cycle required for the switchability test.) After 6 × 10^5 s (~7 days), the cell A resistance had gradually increased to 116 kΩ but the device remained switchable (according to the test on surrogate cells B, C, *etc.*). After that, the cell A resistance dropped rapidly, indicating a "loss of memory". Eventually, failure occurred in the sense that the cell could no longer be switched to the LRS (again, according to the switchability test on another virgin surrogate cell D) after 2 × 10^6 s (~23 days). It should be noted that the resistance change only occurred when the cell was kept in the HRS; a cell kept in the LRS showed no change in resistance when held at room ambient conditions (see the lower branch data in Figure 5b).

As mentioned already, during the above retention test, cell A was not disturbed by the voltage sweep cycle; the switchability was established through testing the surrogates. If instead the same cell is periodically disturbed and tested for switchability, then its R_{HRS} increase is much faster, and the failure comes sooner. Figure 5c shows such a cell having an initial R_{HRS} ~ 51 kΩ at 0.2 V, which increased to 1.2 MΩ after 15 days during which it was switched merely 3 times. When checked on day 20, the cell already lost its memory and was not able

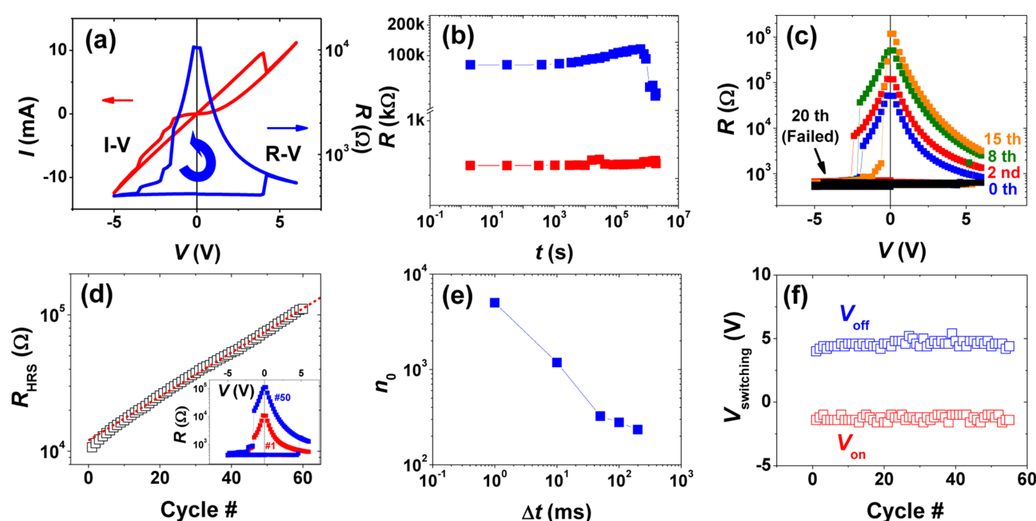

Figure 5. (a) Current (I)−voltage (V) and resistance (R)−voltage (V) characteristic of 80% SiO_2:20% Pt nanometallic device. (b) Resistance retention (read at 0.2 V) in ambient air for HRS (blue) and LRS (red); HRS rolls off at around 10^6 s. (c) Cell held in HRS and switched 3 times (switching $R-V$ curves shown) during first 15 days; failure after 20 days. (d) Exponential increase of HRS resistance during consecutive 60 switching cycles (0 V → 5 V → 6 V → −5 V → 0 V, cycle duration $\Delta t \sim 1$ s). Inset: $R-V$ curves of 1st and 50th cycle, respectively. (e) Degradation factor n_0 *vs* pulse duration Δt. Negative slope ∼1 indicates that degradation depends on total time under electric loading. (f) Switching voltages (V_{off} and V_{on}) remain constant during consecutive switching cycles.

to switch to the HRS after on-switching. This indicates that repeated switching, even just a few times, can cause much more degradation if the cell is held in the HRS. To further investigate the effect of repeated switching, we conducted the voltage sweep cycle without interruption in the so-called fatigue or endurance test. As shown by the $R-V$ curves in the inset of Figure 5d, the HRS of the first cycle differs significantly from that of the 50th cycle. (The switching voltages are relatively constant: off-switching at 4 V and on-switching at −1 V, as is the LRS remaining at 420 Ω.) The R_{HRS} increased (Figure 5d) exponentially with the number of cycle n: $R_{HRS} = R_0 \times \exp(n/n_0)$ with $n_0 = 27$, meaning doubling R_{HRS} every 19 cycles. To investigate whether the HRS degradation is dependent on the voltage sweep period Δt, we repeated the fatigue test at other Δt and analyzed the results in terms of n_0 used in the exponential "law". As shown in Figure 5e, a faster pulse yielded a larger n_0 and *vice versa*. However, since the initial slope of log n_0 *versus* log Δt is close to −1, meaning $n_0 \Delta t \sim$ constant, the HRS degradation (at least during fast switching) is dependent on the total time ($n\Delta t$) only, following $R_{HRS} = R_0 \times \exp(t/t_0)$ with $t_0 \sim 10^4$ s. This result may be regarded as representative of "dynamic" degradation caused by both an internal field (due to the trapped charge in the HRS) and an external field (due to the voltage sweep). Compared to "static" degradation in Figure 5b ($t_0 \sim 1.8 \times 10^6$ s) caused by only an internal field without an external field, dynamic degradation is much faster. Lastly, in contrast to the exponential rise of R_{HRS} (Figure 5d), switching voltages (V_{off} and V_{on}) remained unchanged during sweeping cycles (Figure 5f). This is unlike the case of Tsuruoka *et al.*, in which large variations in switching voltage with environment were found for the Cu/SiO_2/Pt and Cu/Ta_2O_5/Pt cells.[18]

Temperature Dependence of R, ε_r', and tan δ. The DC resistance and lower-frequency dielectric spectra of the HRS of a SiO_2:Pt film shown in Figure 6 all display a pronounced temperature dependence. As-fabricated devices in this study had a $R_{HRS} \sim 200$ kΩ, which degraded to ∼1 MΩ after three months. This change is reversible: as shown in Figure 6a, it decreased to 35 kΩ at just above 100 °C. R_{HRS} continued to gradually decrease when the cell was heated above 100 °C, reaching ∼20 kΩ at 175 °C. After cooling, it recovered the as-fabricated resistance. The above behavior suggests a two-stage process: the first stage (the low-temperature part) is related to the loss of water; the second stage (the high-temperature part) reflects the negative dR/dT property (*i.e.*, increased conductivity) common to all insulators. Relative dielectric constant (the real part, ε_r', Figure 6b) also appears to undergo a large decrease above 100 °C as water evaporates, especially at low frequency. The much stronger frequency dependence below 100 °C signals a contribution of a polar species, presumably H_2O or OH, that undergoes relatively slow dielectric relaxations compared to intrinsic ionic and electronic contributions. The influence of water is too implicated in Figure 6c by the large tan δ, which can arise from both dielectric loss and conductivity loss. At low temperature and high frequency (100 kHz), it already reaches 0.5 even though the DC resistance is still high (>1 MΩ, Figure 6a); most likely, the dominant contribution here comes from dielectric relaxation of water. Remarkably, as the temperature increases, tan δ continues to increase at least up to 100 °C despite the expected evaporative loss of water which should reduce tan δ. This suggests that the thermally activated dielectric relaxation of H_2O

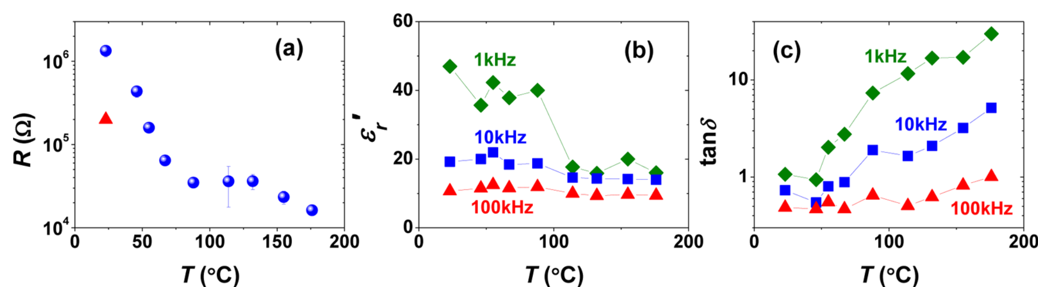

Figure 6. Temperature dependence of (a) HRS DC resistance, (b) real part of dielectric constant ε_r', and (c) tangent loss (tan δ) of 80% SiO_2:20% Pt device during heating; before the test, the device was in ambient air for 3 months. Red triangle in (a): data of as-fabricated device, which coincide with the extrapolation of resistance data above 100 °C.

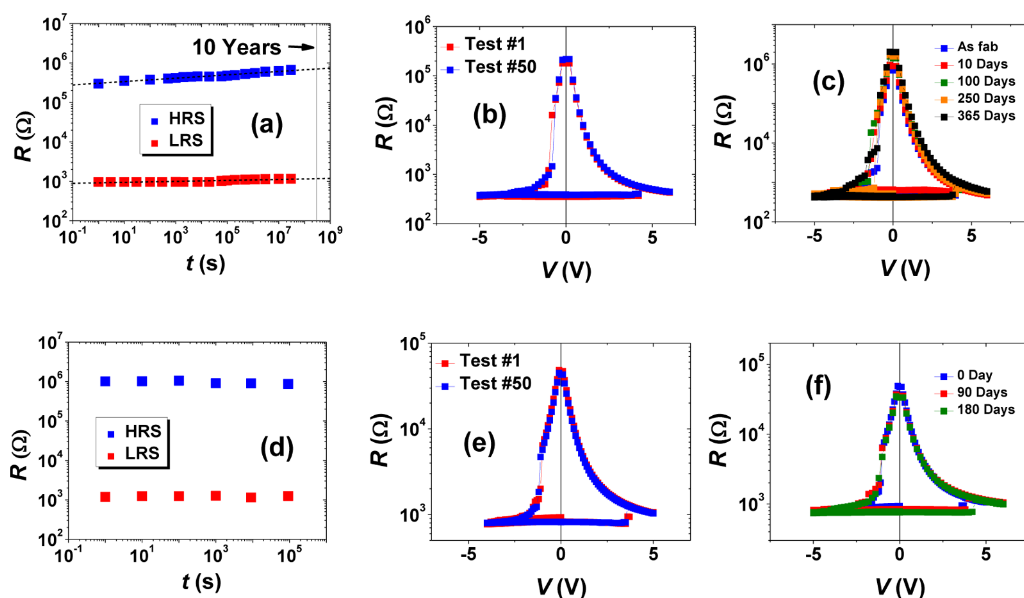

Figure 7. Robust devices made of 93% Si_3N_4:7% Cr showing (a) resistance retention with extrapolated HRS and LRS resistance to 10 years; (b) *R*−*V* curves of 1st and 50th cycles over consecutive 50 cycles, and (c) *R*−*V* curves taken over 365 days, with almost identical curves in (b) and (c). Likewise, robust devices made of Al_2O_3-capped 80% SiO_2:20% Pt showing (d) resistance retention over 10^5 s; (e) *R*−*V* curves of 1st and 50th cycles over consecutive 50 cycles, and (f) *R*−*V* curves taken over 180 days, with almost identical curves in (d) and (e).

molecule is much more temperature-sensitive than water evaporation. (A drop in tan δ reflecting the water loss eventually occurs at ∼100 °C in the spectra of 10 and 100 kHz in Figure 6c.) Lastly, above 120 °C, tan δ increases again at all frequencies in coincidence with the decreased DC resistance, which is consistent with our earlier suggestion of the negative d*R*/d*T* property (*i.e.*, increasing conductivity) common to all insulators. The "intrinsic" background dielectric constant may be taken as $\varepsilon_r' \sim 10$ seen in the high-frequency, high-temperature limit, which is considerably higher than that of porous SiO_2 (3.8 for fused SiO_2) because of the metal content. In the literature, other water-containing SiO_2 films are also known to have a higher dielectric constant than pristine silica; this is generally attributed to the easily polarizable OH groups (such as Si−OH) that populate the films.[45]

Robust Devices. Robust electric characteristics were observed using 93% Si_3N_4:7% Cr films, 95% Si_3N_4:5% Pt films, Al_2O_3-capped 80% SiO_2:20% Pt films, and 80% SiO_2:20% Pt films with $SrRuO_3$ bottom electrodes. Retention data in Figure 7a of a 93% Si_3N_4:7% Cr cell show that HRS degradation is largely avoided. (If the data are extrapolated to 10 years, they can easily fulfill the requirement for data storage of a good memory.) Supporting evidence also came from *R*−*V* loops shown in Figure 7b: the 50th loop is indistinguishable from the first loop. Indeed, even after 1 year, the *R*−*V* curve hardly changed despite the fact that the cell had been periodically tested, as shown in Figure 7c. Likewise, a capped SiO_2:Pt device showed the same robust behavior: no HRS change in retention (Figure 7d) and no change in the *R*−*V* loops in either cycle tests (Figure 7e) or during storage (Figure 7f). (The Al_2O_3 capping layer was deposited over the film and the top electrode. Before electric testing, the capping layer was poked by the probe tip under a small voltage to establish electric contact to the top electrode.) Similar data for 95% Si_3N_4:5% Pt with Mo bottom electrode and for SiO_2:Pt with $SrRuO_3$ bottom electrode showing no degradation

are provided in Figures S3 and S4 of the Supporting Information.

DISCUSSION

It is obvious that (a) moisture is connected to the film and device degradation; (b) the severity is influenced by the intrinsic physicochemical nature of the film and/or nanoporosity; (c) the moisture effect can be "blocked" by having a dense capping layer; (d) electric fields, both internal and external, accelerate degradation; and (e) bottom electrode, being Mo or $SrRuO_3$, has a decisive influence on the degradation effect. In the above, (a−c) are strongly correlated to wetting: all three nondegrading devices described in Figure 7 and Figure S2 (in Supporting Information) have relatively high wetting angles on the films, whereas rapidly degrading SiO_2:Pt films are nearly completely wetting. The measured intrinsic water wetting angles θ_e of dense dielectrics studied here are only slightly different, increasing from 50 to 60° in the order of SiO_2, Al_2O_3, and Si_3N_4. Intrinsic wetting properties reflect the physical chemistry of the materials pair (water and dielectric) in contact.[46,47] In our case, ionic characters of both Si−O and Al−O bonds make SiO_2 and Al_2O_3 relatively hydrophilic; meanwhile, Si−O bonds very likely are also present on the surface of Si_3N_4, making it too similarly hydrophilic. This suggests that intrinsic physicochemical nature is similar for all films in the present study, thus it is not a differentiating factor for degradation.

On the other hand, the relatively small difference in θ_e can be overwhelmed by the influence of surface roughness, caused by nanoporosity, which varies greatly between films. Porosity (volume fraction P) increases the effective contact area by a (roughness) factor $r = 1 + 2P > 1$ (see Supporting Information). According to the Wenzel equation

$$\cos \theta_r^w = r \cos \theta_e$$

$r > 1$ leads to a smaller wetting angle θ_r^w on a porous rough surface than that on a dense smooth surface. For SiO_2:Pt films with $P = 0.5$, we estimate $r = 2$, which predicts complete wetting. Nearly complete wetting was indeed observed in Figure 4a. For other films, nanoporosity is too small to significantly affect wetting, which is also in agreement with our observations in Figure 4b−f. Therefore, we may conclude that, in our study, it is nanoporosity that is the direct cause for degradation. Moreover, since some nanoporosity always exists even in nondegrading films, we believe it is interconnected nanoporosity which penetrates deep inside the films that causes degradation. In addition, films with a small P probably do not have such penetrating nanoporosity, hence they do not suffer from moisture-induced degradation. This scenario is also consistent with the outcome of surface capping: once the surface is capped by a dense film, moisture penetration apparently stops.

We next examine the possible mechanisms *via* which moisture aided by an internal or external electric field can cause R_{HRS} to increase when the bottom electrode is Mo but not when the bottom electrode is $SrRuO_3$. Note that this occurs without any significant change in R_{LRS} and switching voltages. The latter observation rules out any effect on the interface since any rise in the interface resistance must be reflected in a corresponding rise in the switching voltage, as the actual voltage across the film to trigger switching must become less due to voltage sharing by the interface resistance.[31] This leaves distributed degradation throughout the film the more likely cause for the R_{HRS} increase. We propose this occurs in two steps: (1) H_2O attraction to the film interior *via* dielectrophoresis,[48] and (2) H_2O-mediated Mo oxidation and silicic acid formation, creating negative charge centers $(OH)^-$. Concerning step (1), in dielectrophoresis, an object (such as H_2O molecule) that has a higher dielectric constant than the surrounding experiences a force in the direction of increasing field (absolute) magnitude. If there is only an internal field E_{int}, the force is proportional to the gradient of E_{int}^2, so H_2O should migrate toward the centers of this field, which are located inside the film at trapped charges (electrons) at the so-called negative-U centers.[32] (In nanometallic memory, filling these negative-U centers by trapped charge is responsible for the LRS-to-HRS transition. Conversely, emptying these centers by detrapping is responsible for the HRS-to-LRS transition.) When a uniform AC/DC external field E_{ext} is added, the net force is proportional to the gradient of $E^2 = (E_{int} + E_{ext})^2$, that is, the gradient of $E_{int}^2 + 2E_{int}E_{ext}$.[48] So it always enhances dielectrophoresis along some direction of E_{int}, pointing to the center of E_{int}: the trapped charge. Therefore, an external field merely amplifies the dielectrophoretic force and accelerates moisture-caused degradation without otherwise altering the direction.

Concerning step (2), we envision a H_2O-mediated redox reaction resulting in electron transfer from Mo to SiO_2 in the following reaction: $Mo + SiO_2 + 2H_2O = Mo^+ + [Si(OH)_4]^-$. Here, Mo oxidation with attendant SiO_2 reduction is aided by hydroxyl formation. Moreover, we believe it is further aided by either a mechanical stress due to hydrolysis strain, or $E_{int} + E_{ext}$, both of which deform the SiO_2 network, thus facilitating Si−O−Si bond rupture[49,50] followed by hydroxyl formation. (Obviously, E_{ext} accelerates this reaction. Also, the stress/strain/field gradient is generally larger at the rim of the cell, which may be the reason for the dark ring appearance in Figure 1i) Indeed, the negative-U center itself is often a site of strained bond, which relaxes upon capturing an electron *via* electron−phonon interaction. The net result of steps (1) and (2) is an additional trapped electron at the center of E_{int}, which is already the location of a previously trapped electron as mentioned above. The combined E_{int} of

these two trapped electrons increases the Coulomb barrier that impedes the movement of free electrons, hence a higher R_{HRS}. Note that the "half-cell reactions" (using the term in electrochemistry) in the above overall redox reaction generally do not occur at the same site: the Mo/Mo^+ reaction occurs at the electrode, whereas the $SiO_2-H_2O/[Si(OH)_4]^-$ reaction occurs at the strained Si−O−Si site or negative-U center. The overall reaction involves both half-cell reactions and electron transport between the two sites, which are separated at a distance no more than the film thickness of ∼10 nm.

The above two-step mechanism is consistent with the observation that a positive voltage polarity causes cell darkening (Figure 1g) since it corresponds to a negative voltage on Mo bottom electrode, which favors electron donation by Mo. The mechanism is also consistent with the observation of no degradation with $SrRuO_3$ as the bottom electrode. This is because Ru^{4+} having the low-spin $4d^4$ electron configuration is relatively stable;[51,52] therefore, even though H_2O may still enter the SiO_2:Pt film, there is no redox reaction without electron donation from $SrRuO_3$.

Further insight may be gained from scrutinizing the evolution of R_{HRS} and switching voltages in light of the above picture. To begin with, we note that increase of R_{HRS} with time was also observed in amorphous chalcogenide phase-change memory due to structural relaxation.[53] Characteristically, such relaxation decelerates with time and asymptotically approaches saturation. This is in contrast with the behavior of Figure 5b, which shows acceleration in the log−log plot with no evidence of saturation before a relative sudden drop leading to failure. According to our mechanism, the R_{HRS} increases because of water-facilitated increase in trapped charge and possibly trap sites (negative-U centers). However, water is also known to cause loss of insulating properties of dielectrics, even creating electric shorts.[6] Such water-induced electric degradation is expected to worsen as the internal electric field increases. In our picture, a higher R_{HRS} corresponds to a state of higher internal field, so degradation of the SiO_2 matrix can explain the eventual loss of R_{HRS} after an initial increase. (Another possibility is increased leakage of trapped electrons through tunneling or Frenkel−Poole hopping, which is aided by the increasing density of trapped charge and facilitated by the matrix degradation. Such leakage does not occur in the absence of water infiltration—see Figure 7d and the retention data elsewhere.[32]) After failure, the HRS cell may not be switchable anymore if trapped electrons are stabilized by the water-altered environment, where local bonding could have changed dramatically. (This process can again be aided by the internal electric/mechanical field). So the cell becomes "stuck at the HRS". Alternatively, a failed cell may be returned to the LRS, then becomes "stuck at the LRS" because the dielectric matrix is too leaky to withstand the switching voltage, making it impossible to switch. (The HRS-to-LRS transition requires very little current, so it could precede the above event.) These failure modes have both been described in the previous section. Lastly, the fact that switching voltages in Figure 5f are not changed (until the cell fails) despite the progression of R_{HRS} implies that the additional trapped charge/trapping sites created by water-induced reactions still largely fall into the same energy-level distribution as for the original population. This is because switching in nanometallic RRAM is voltage-controlled depending on the actual voltage in the film and independent of film thickness, area, and temperature.[30−33] For trapped charge/trapping sites of the same energy level, the critical voltage for detrapping/trapping is the same.

In filament-conducting RRAM, moisture was also shown to cause degradation by altering the redox state of the filament-forming species (*e.g.*, Cu/Cu^+): the additional electrochemical driving force in the $Pt/H_2O/Cu/Cu^+$ "cell" lowers the threshold voltage for filament formation and dissolution, hence the switching voltages.[18] This mechanism is not applicable to our study, which witnessed no change in switching voltages when altering environment or temperature. Indeed, the present study supports our claim that nanometallic RRAM is a charge-trapping-controlled switching system,[30−33] unrelated to redox-controlled switching mechanisms and/or filamentary mechanisms that operate in many RRAM.[10−16] On the other hand, moisture-related reliability issues no doubt can arise in other dielectrics which serve as the active layer in most filamentary RRAM: by affecting breakdown, changing carrier concentration, and altering defect thermodynamics[17−21] and moisture-induced charge trapping occurring at resistance-critical junctions of broken filaments could cause a drift of R_{HRS}. However, since charge trapping is not considered important in filamentary RRAM, to the extent that the switching layer indeed has no stored charge, the lack of any internal field could imply less severe moisture-induced problems than observed in our study.

Finally, we return to the observation of nanoporosity formation in these films. As commonly reported in the literature,[4,18,37,38] sputtered dielectric films deposited on an unheated substrate are nanoporous because of sluggish surface diffusion. This situation is exacerbated by co-sputtering of metal species, which may have faster kinetics but are insoluble in dielectrics. Such metal atoms are likely located on the surface of nanopores, like metal catalyst situated on a nanoporous support. As a result, the probability of metal clustering increases with P. Since nanometallicity arises from delocalized electrons placed in an environment of random potential,[31,32,54] metal clustering compared to atomic dispersion is actually detrimental to nanometallicity because it increases the spacing between electron providers (atomically dispersed metal atoms

or metal clusters). This is consistent with our experience. As the amount of nanoporosity increases, the required metal content for resistance switching increases (see Figure S5 in Supporting Information). In this respect, the most "efficient" nanometallic films having the lowest metal content requirement should also be the most moisture resistant—they have the lowest nanoporosity.

CONCLUSIONS

This study has determined the following. (1) When electron-donating Mo is used as the bottom electrode, moisture induces physical and electric/dielectric changes in SiO_2:Pt nanometallic RRAM, including decoloration and increases in dielectric constant and R_{HRS}, but not R_{LRS}. However, unlike filamentary RRAM, switching voltages remain unchanged in these devices. (2) Moisture penetrates *via* nanoporosity in the films, which can become almost completely water wetting due to nanoporosity-caused surface roughening. (3) Internal electric fields attract H_2O molecules *via* dielectrophoresis, and motivate redox reaction causing Mo oxidation and SiO_2 reduction, which traps electrons at Si−OH, providing increasingly stronger Coulomb repulsion, thus a higher R_{HRS}. This process is greatly enhanced by an external field. (4) With lower nanoporosity or a dense capping layer, wetting, decoloration and device degradation can be avoided, rendering robust switching and memory retention readily feasible in nanometallic RRAM. The same can also be achieved by replacing Mo with an oxidation-resistant electrode such as $SrRuO_3$.

EXPERIMENTAL METHODS

Device Fabrication. All devices were fabricated on SiO_2/Si substrates (Figure 1a). Substrates were cleaned by acetone and isopropyl alcohol followed by heating at 150 °C in vacuum for 30 min in a sputter chamber (vacuum level: 3×10^{-7} Torr). After cooling to room temperature, a bottom Mo electrode was deposited by DC sputtering before a nanometallic film was deposited by RF magnetron co-sputtering using targets of a metal (Pt or Cr) and an insulator (SiO_2 or Si_3N_4) (DC power = 300 W; RF power = 200 W for insulator SiO_2 or Si_3N_4; 10−30 W for Pt or Cr; no vacuum break between these steps). Next, top Pt electrodes were RF sputter-deposited (RF power = 30 W) and patterned (having a circular area of various sizes) lithographically or by a shadow mask. On some devices, a capping layer of 4 nm thick Al_2O_3 was deposited after device fabrication, by atomic layer deposition (ALD) under the following condition: precursor, trimethylaluminum; oxidant, H_2O; wafer temperature, 150 °C. For a comparative study, another set of samples used in a previous research,[30,31] with the same SiO_2:Pt composition and Pt top electrode but $SrRuO_3$ (SRO) bottom electrode deposited by pulse laser deposition, was also investigated.

Characterization. For density determination, nanometallic films on MgO substrates were studied by Rutherford backscattered spectrometry (RBS, NEC Minitandem Ion Accelerator), and the composition and density distributions were obtained using the simulation software (SIMNRA). Density was also confirmed using X-ray reflectometry (Bruker D8 Discover) using films on Si wafers. DC electric measurements were conducted using a semiconductor parameter analyzer (SPA, Keithley 237), while AC impedance spectroscopy was studied using an impedance analyzer (Gamry G750). For these studies, samples were placed on a probe station (Signatone S1160) and a voltage was applied between the top and the bottom electrodes. (Current flowing from the top electrode to the bottom electrode is considered positively biased.) A homemade electric hot plate was used to heat the sample with the temperature monitored by a thermocouple nearby. For IR spectroscopy, nanometallic films were deposited on IR-transparent KBr substrates and measured using a Nicolet Nexus 470 FTIR spectrometer. Static contact angles of water were measured on various films/materials, without patterned top electrodes, by a rame-hart goniometer (model 200) using 2.0 μL droplets and averaged over several locations. Unless otherwise noted, characterization was conducted in air at room temperature.

Conflict of Interest: The authors declare no competing financial interest.

Acknowledgment. This research was supported by the U.S. National Science Foundation (Grant No. DMR-11-04530, primarily, and DMR-09-07523 and DMR-11-20901, in part).

Supporting Information Available: A quantitative estimation of nanopore size and roughness—including atomic force microscopy, IR spectra of 93% Si_3N_4:7% Cr, device properties of 95% Si_3N_4:5% Pt (Mo BE) and 80% SiO_2:20% Pt ($SrRuO_3$), and schematic effect of film density on optimal metal concentration and film thickness. This material is available free of charge *via* the Internet at http://pubs.acs.org.

REFERENCES AND NOTES

1. Ngaruiya, J. M.; Venkataraj, S.; Drese, R.; Kappertz, O.; Pedersen, T. P. L.; Wuttig, M. Preparation and Characterization of Tantalum Oxide Films Produced by Reactive DC Magnetron Sputtering. *Phys. Status Solidi A* **2003**, *198*, 99–110.
2. Fang, Q.; Zhang, J. Y. Nano-porous TiN Thin Films Deposited by Reactive Sputtering Method. *Int. J. Inorg. Mater.* **2001**, *3*, 1193–1196.
3. Cyviene, J.; Milcius, D.; Laukaitis, G. Porosity Evaluation of TiO_2 Thin Films Deposited Using Pulsed DC-Magnetron Sputtering. *Mater. Sci.* **2009**, *15*, 103–107.
4. Kim, J. H.; Chung, K. W. Microstructure and Properties of Silicon Nitride Thin Films Deposited by Reactive Bias Magnetron Sputtering. *J. Appl. Phys.* **1998**, *83*, 5831–5839.
5. Zhao, Y.; Toyama, M.; Kita, K.; Kyuno, K.; Toriumi, A. Moisture-Absorption-Induced Permittivity Deterioration and Surface Roughness Enhancement of Lanthanum Oxide Films on Silicon. *Appl. Phys. Lett.* **2006**, *88*, 072904.
6. Wang, C. T.; Wu, C. L. Electrical Sensing Properties of Silica Aerogel Thin Films to Humidity. *Thin Solid Films* **2006**, *496*, 658–664.
7. Kim, W.; Javey, A.; Vermesh, O.; Wang, O.; Li, Y. M.; Dai, H. J. Hysteresis Caused by Water Molecules in Carbon Nanotube Field-Effect Transistors. *Nano Lett.* **2003**, *3*, 193–198.
8. Emel'yanov, A. M. Water-Related Charge Carrier Traps in Thermal Silicon Dioxide Films Prepared in Dry Oxygen. *Phys. Solid State* **2010**, *52*, 1131–1137.
9. Waser, R.; Dittmann, R.; Staikov, G.; Szot, K. Redox-Based Resistive Switching Memories: Nanoionic Mechanisms, Prospects, and Challenges. *Adv. Mater.* **2009**, *21*, 2632–2663.
10. Yang, Y.; Gao, P.; Gaba, S.; Chang, T.; Pan, X.; Lu, W. Observation of Conducting Filament Growth in Nanoscale Resistive Memories. *Nat. Commun.* **2012**, *3*, 732.
11. Waser, R.; Aono, M. Nanoionics-Based Resistive Switching Memories. *Nat. Mater.* **2007**, *6*, 833–840.
12. Kwon, D.-H.; Kim, K. M.; Jang, J. H.; Jeon, J. M.; Lee, M. H.; Kim, G. H.; Li, X.-S.; Park, G.-S.; Lee, B.; Han, S.; *et al.* Atomic Structure of Conducting Nanofilaments in TiO_2 Resistive Switching Memory. *Nat. Nanotechnol.* **2010**, *5*, 148–153.

13. Lee, D.; Choi, H.; Sim, H.; Choi, D.; Hwang, H.; Lee, M. J.; Seo, S. A.; Yoo, I. K. Resistance Switching of the Nonstoichiometric Zirconium Oxide for Nonvolatile Memory Applications. *IEEE Electron Device Lett.* **2005**, *26*, 719–721.
14. Lin, C.-Y.; Wu, C.-Y.; Wu, C.-Y.; Lin, C.-C.; Tseng, T.-Y. Memory Effect of RF Sputtered ZrO_2 Thin Films. *Thin Solid Films* **2007**, *516*, 444–448.
15. Chai, Y.; Wu, Y.; Takei, K.; Chen, H.-Y.; Yu, S.; Chan, P. C. H.; Javey, A.; Wong, H. S. P. Nanoscale Bipolar and Complementary Resistive Switching Memory Based on Amorphous Carbon. *IEEE Trans. Electron Devices* **2011**, *58*, 3933–3939.
16. Karpov, I. V.; Kostylev, S. A. SET to RESET Programming in Phase Change Memories. *IEEE Electron Device Lett.* **2006**, *27*, 808–810.
17. Peterson, C. A.; Workman, R. K.; Sarid, D.; Vermeire, B.; Parks, H. G.; Adderton, D.; Maivald, P. Effects of Moisture on Fowler−Nordheim Characterization of Thin Silicon-Oxide Films. *J. Vac. Sci. Technol., A* **1999**, *17*, 2753–2758.
18. Tsuruoka, T.; Terabe, K.; Hasegawa, T.; Valov, I.; Waser, R.; Aono, M. Effects of Moisture on the Switching Characteristics of Oxide-Based, Gapless-Type Atomic Switches. *Adv. Funct. Mater.* **2012**, *22*, 70–77.
19. Hoflund, G. B.; Corallo, G. R. Electron-Energy-Loss Study of the Oxidation of Polycrystalline Tin. *Phys. Rev. B* **1992**, *46*, 7110–7120.
20. Nagashima, K.; Yanagida, T.; Oka, K.; Kanai, M.; Klamchuen, A.; Kim, J.-S.; Park, B. H.; Kawai, T. Intrinsic Mechanisms of Memristive Switching. *Nano Lett.* **2011**, *11*, 2114–2118.
21. Nagashima, K.; Yanagida, T.; Oka, K.; Kanai, M.; Klamchuen, A.; Rahong, S.; Meng, G.; Horprathum, M.; Xu, B.; Zhuge, F.; *et al.* Prominent Thermodynamical Interaction with Surroundings on Nanoscale Memristive Switching of Metal Oxides. *Nano Lett.* **2012**, *12*, 5684–5690.
22. Lee, S.; Lee, J.; Park, J.; Choi, Y.; Yong, K. Resistive Switching WOx-Au Core−Shell Nanowires with Unexpected Nonwetting Stability Even When Submerged under Water. *Adv. Mater.* **2012**, *24*, 2418–2423.
23. Gomes, H. L.; Rocha, P. R. F.; Kiazadeh, A.; De Leeuw, D. M.; Meskers, S. C. J. Anomalous Temperature Dependence of the Current in a Metal-Oxide-Polymer Resistive Switching Diode. *J. Phys. D: Appl. Phys.* **2011**, *44*, 025103.
24. Knorr, N.; Wirtz, R.; Rosselli, S.; Nelles, G. Field-Absorbed Water Induced Electrochemical Processes in Organic Thin Film Junctions. *J. Phys. Chem. C* **2010**, *114*, 15791–15796.
25. Shoute, L. C. T.; Pekas, N.; Wu, Y.; McCreery, R. L. Redox Driven Conductance Changes for Resistive Memory. *Appl. Phys. A: Mater. Sci. Process.* **2011**, *102*, 841–850.
26. Lee, S.; Kim, W.; Yong, K. Overcoming the Water Vulnerability of Electronic Devices: A Highly Water-Resistant ZnO Nanodevice with Multifunctionality. *Adv. Mater.* **2011**, *23*, 4398–4402.
27. Chang, W.-Y.; Cheng, K.-J.; Tsai, J.-M.; Chen, H.-J.; Chen, F.; Tsai, M.-J.; Wu, T.-B. Improvement of Resistive Switching Characteristics in TiO_2 Thin Films with Embedded Pt Nanocrystals. *Appl. Phys. Lett.* **2009**, *95*, 042104.
28. Gao, B.; Zhang, H. W.; Yu, S.; Sun, B.; Liu, L. F.; Liu, X. Y.; Wang, Y.; Han, R. Q.; Kang, J. F.; Yu, B.; Wang, Y. Y. Oxide-Based RRAM: Uniformity Improvement Using a New Material-Oriented Methodology. *Symp. VLSI Technol.* **2009**, 30.
29. Tsunoda, K.; Kinoshita, K.; Noshiro, H.; Yamazaki, Y.; Iizuka, T.; Ito, Y.; Takahashi, A.; Okano, A.; Sato, Y.; Fukano, T.; *et al.* Low Power and High Speed Switching of Ti-Doped NiO ReRAM under the Unipolar Voltage Source of Less than 3 V. *IEEE Int. Electron Devices Meet.* **2007**, 767.
30. Chen, A. B. K.; Kim, S. G.; Wang, Y.; Tung, W.-S.; Chen, I. W. A Size-Dependent Nanoscale Metal-Insulator Transition in Random Materials. *Nat. Nanotechnol.* **2011**, *6*, 237–241.
31. Chen, A. B. K.; Choi, B. J.; Yang, X.; Chen, I. W. A Parallel Circuit Model for Multi-state Resistive-Switching Random Access Memory. *Adv. Funct. Mater.* **2012**, *22*, 546–554.
32. Choi, B. J.; Chen, A. B. K.; Yang, X.; Chen, I. W. Purely Electronic Switching with High Uniformity, Resistance Tunability, and Good Retention in Pt-Dispersed SiO_2 Thin Films for ReRAM. *Adv. Mater.* **2011**, *23*, 3847–3852.
33. Yang, X.; Chen, I. W. Dynamic-Load-Enabled Ultra-low Power Multiple-State RRAM Devices. *Sci. Rep.* **2012**, *2*, 744.
34. Oh, M. S.; Yang, B. S.; Lee, J. H.; Oh, S. H.; Lee, U. S.; Kim, Y. J.; Kim, H. J.; Huh, M. S. Improvement of Electrical and Optical Properties of Molybdenum Oxide Thin Films by Ultralow Pressure Sputtering Method. *J. Vac. Sci. Technol., A* **2012**, *30*, 031501.
35. Bhosle, V.; Tiwari, A.; Narayan, J. Epitaxial Growth and Properties of MoO_x ($2 < x < 2.75$) Films. *J. Appl. Phys.* **2005**, *97*, 083539.
36. Greenwood, N. N.; Earnshaw, A. *Chemistry of the Elements*; Pergamon Press: Oxford, 1984.
37. Pliskin, W. A.; Lehman, H. S. Structural Evaluation of Silicon Oxide Films. *J. Electrochem. Soc.* **1965**, *112*, 1013–1019.
38. Abeles, B. Granular Metal Films. In *Applied Solid State Science*; Wolfe, R., Ed.; Academic: New York: 1976; Vol. 6, pp 1−117.
39. Doo, V. Y.; Nichols, D. R.; Silvey, G. A. Preparation and Properties of Pyrolytic Silicon Nitride. *J. Electrochem. Soc.* **1966**, *113*, 1279–1281.
40. Takeuchi, M.; Bertinetti, L.; Martra, G.; Coluccia, S.; Anpo, M. States of H_2O Adsorbed on Oxides: An Investigation by Near and Mid Infrared Spectroscopy. *Appl. Catal., A* **2006**, *307*, 13–20.
41. Davis, K. M.; Tomozawa, M. An Infrared Spectroscopic Study of Water-Related Species in Silica Glasses. *J. Non-Cryst. Solids* **1996**, *201*, 177–198.
42. Thomas, R. R.; Kaufman, F. B.; Kirleis, J. T.; Belsky, R. A. Wettability of Polished Silicon Oxide Surfaces. *J. Electrochem. Soc.* **1996**, *143*, 643–648.
43. Tricoli, A.; Righettoni, M.; Pratsinis, S. E. Anti-fogging Nanofibrous SiO_2 and Nanostructured SiO_2-TiO_2 Films Made by Rapid Flame Deposition and *In Situ* Annealing. *Langmuir* **2009**, *25*, 12578–12584.
44. Chen, I. W.; Rosenflanz, A. A Tough SiAlON Ceramic Based on α-Si_3N_4 with a Whisker-like Microstructure. *Nature* **1997**, *389*, 701–704.
45. Won, S.-J.; Jung, H.-S.; Suh, S.; Choi, Y. J.; Lee, N.-I.; Hwang, C. S.; Kim, H. Growth and Electrical Properties of Silicon Oxide Grown by Atomic Layer Deposition Using Bis(ethylmethyl-amino)silane and Ozone. *J. Vac. Sci. Technol., A* **2012**, *30*, 01A126.
46. Menon, M.; Chen, I. W. Reaction Densification of α-SiAlON. 1. Wetting Behavior and Acid-Based Reactions. *J. Am. Ceram. Soc.* **1995**, *78*, 545–552.
47. Hwang, S. L.; Chen, I. W. Reaction Hot-Pressing of α'-SiAlON and β'-SiAlON Ceramics. *J. Am. Ceram. Soc.* **1994**, *77*, 165–171.
48. Jones, T. B. *Electromechanics of Particles*; Cambridge University Press: New York, 1995.
49. Michalske, T. A.; Freiman, S. W. A Molecular Mechanism for Stress-Corrosion in Vitreous Silica. *J. Am. Ceram. Soc.* **1983**, *6*, 284–288.
50. Jacobs, D. S.; Chen, I. W. Mechanical and Environmental Factors in the Cyclic and Static Fatigue of Silicon Nitride. *J. Am. Ceram. Soc.* **1994**, *77*, 1153–1161.
51. Mamchik, A.; Chen, I. W. Magnetic Impurities in Conducting Oxides. I. $(Sr_{1-x}La_x)(Ru_{1-x}Fe_x)O_3$ System. *Phys. Rev. B* **2004**, *70*, 104409.
52. Mamchik, A.; Dmowski, W.; Egami, T.; Chen, I. W. Magnetic Impurities in Conducting Oxides. II. $(Sr_{1-x}La_x)(Ru_{1-x}Fe_x)O_3$ System. *Phys. Rev. B* **2004**, *70*, 104410.
53. Karpov, I. V.; Mitra, M.; Kau, D.; Spadini, G.; Kryukov, Y. A.; Karpov, V. G. Fundamental Drift of Parameters in Chalcogenide Phase Change Memory. *J. Appl. Phys.* **2007**, *102*, 124503.
54. Egami, T. Random Materials: Localization on the Nanoscale. *Nat. Nanotechnol.* **2011**, *6*, 199–200.